Polar and Phase Domain Walls in Weyl Semimetallic $MoTe_2$: New Paradigm for Topological Interfacial States

Fei-Ting Huang[1], Seong Joon Lim[1], Sobhit Singh[2], Jinwoong Kim[2], Lunyong Zhang[3], Jae-Wook Kim[1], Ming-Wen Chu[4], Karin M. Rabe[2], David Vanderbilt[2] and Sang-Wook Cheong[1*]

[1]Rutgers Center for Emergent Materials and Department of Physics and Astronomy, Rutgers University, Piscataway, New Jersey 08854, USA

[2] Department of Physics and Astronomy, Rutgers University, Piscataway, New Jersey 08854, USA,

[3]Laboratory for Pohang Emergent Materials and Max Plank POSTECH Center for Complex Phase Materials, Pohang University of Science and Technology, Pohang 37673, Republic of Korea

[4]Center for Condensed Matter Sciences, National Taiwan University, Taipei 106, Taiwan

Abstract

Much of the dramatic growth in research on topological materials has focused on topologically protected surface states. While the domain walls of topological materials such as Weyl semimetals with broken inversion or time-reversal symmetry can provide a new paradigm for exploring topological interfacial states, such investigations have received little attention to date. Here, utilizing in-situ cryogenic transmission electron microscopy combined with first-principles calculations, we discover intriguing domain-wall structures in $MoTe_2$, both between polar variants of the low-temperature(T) Weyl phase, and between this and the high-T higher-order topological phase. We demonstrate how polar domain walls can be manipulated with electron beams, and show that phase domain walls tend to form superlattice-like structures along the *c* axis. Scanning tunneling microscopy indicates a possible signature of a conducting hinge state at phase domain walls. Our results open new avenues for investigating topological interfacial states and unveiling multifunctional aspects of domain walls in topological materials.

In the past decade, an explosion of research has focused on a sweeping search of candidate materials that may harbor topologically-protected surface states[1-6]. Topologically

protected surface states of massless relativistic quasiparticles are their key features, which could be two-dimensional (2D) Dirac points on the surfaces of topological insulators (TIs), or Fermi-arc surface states attached to the bulk Weyl points in the case of three-dimensional topological Weyl semimetals (WSMs)[3,4,6]. The manipulation of these surface states through homo/hetero-structures between topological phases promises functionalities going beyond those of their constituents with important applications such as dissipationless electronics[7-10]. For example, when these topological insulators are interfaced with superconductors, the emergent zero-energy Majorana fermion states at the boundaries can be utilized for topological quantum computation[7]. The Veselago lens, which is the electronic lenses going beyond the diffraction limit, could also be realized through a single *p-n* junction in WSM[9]. However, despite the concept of topological protection, utilizing topological surface states still remains highly challenging due to the chemical/structural/electronic complexity of the surfaces, which may undergo surface reconstruction or chemical adsorption[11-13]. Alternatively, a large number of known topological materials have domains and domain walls (DWs) associated with broken symmetries. While DWs of topological materials can thus provide a new hunting ground to explore new topological interfacial state, limited work has been done to date[14-16].

Among those topological materials, WSMs can be generated quite generally in a semimetallic crystal with large spin-orbit coupling by breaking either time-reversal or space-inversion symmetry[3,6]. Magnetic WSMs remain challenging due to their subtle magnetic band structure calculations. On the other hand, a considerable number of WSMs with broken space-inversion symmetry have been theoretically and experimentally identified, including transition-metal dichalcogenide (TMD) orthorhombic (Mo,W)Te_2[17,18], transition-metal monopnictide (Ta, Nb)(As, P) family[4,5,19], and the RAlGe (R = rare earth) family[20,21]. An appealing aspect of these WSMs is that they also crystallize in polar crystallographic structures with a unique polar axis along which the two opposite directions are distinguishable, and thus they are polar WSMs. Note that since they are highly conducting at low frequencies, these polar WSMs belong to the so-called polar metals that have recently drawn much attention in the ferroelectric community[22-24]. In principle, itinerant electron screening in a (semi)metal might rule out the necessity of electrostatically-driven domain formation due to the fundamental incompatibility of polarity and metallicity, but the existence of polar domains, formed by local bonding preferences, is still possible since this mechanism is insensitive to the presence of charge carriers[22]. In this context,

exploring the domains and the DWs in polar Weyl semimetal would be particularly important because the Weyl points and Fermi-arc connectivity can be manipulated via domain reorientation or locally modified order parameters at these DWs[25-28]. Here we choose TMD $MoTe_2$, which has recently drawn immense attention due to its phase tunability and unique physical properties, such as extremely large magnetoresistance[29], superconductivity[30,31], high-order topology[32-34] and the novel type-II WSM phase[17,18]. Utilizing in-situ cryogenic transmission electron microscopy (TEM) and low-T scanning tunneling microscope (STM), we unveil, for the first time, experimentally intriguing structures of polar and phase DWs between topologically distinct phases in such a polar Weyl semimetal.

Unique layered structures of the Weyl semimetal and the high-order topological semimetal phases of $MoTe_2$

Depending on the crystal structure, $MoTe_2$ can be either in the semiconducting 2H or the semimetallic 1T' phase at room temperature. 1T'-$MoTe_2$ undergoes a first-order type structural transition from a monoclinic ($P2_1/m$, S.G. 11) to an orthorhombic polar T_d ($Pmn2_1$, S.G. 31) phase at a critical temperature (T_c) of ~260 K (Supplementary Fig. S1). T_d-$MoTe_2$ is a rare simultaneous example of a material with superconductivity[30,31], a polar nature[35] (Supplementary section 1), and a topologically nontrivial band structure[17,18], whereas 1T'-$MoTe_2$ is a non-polar high-order topological material in which the 1D hinge instead of 2D surfaces host topologically protected conducting modes[32-34]. The type-II WSM transition occurs in the polar T_d phase due to the requirement of broken inversion symmetry in this nonmagnetic system[17,36,37]. Notably, the inversion symmetry together with the time-reversal symmetry protects the higher-order topological phase in the nonpolar 1T'-$MoTe_2$[32-34]. Despite the apparent dissimilarity in the electronic structure, the 1T' and T_d-$MoTe_2$ phases can, in fact, be considered different stacks of the similar Te-Mo-Te layers. Figure 1a illustrates the basic unit, where the off-centered Mo atoms (blue spheres) move towards each other to form metallic zigzag chains (bold red lines) running along the *a* axis. Consequently, the Te octahedra are deformed with two possible orientations, denoted as P (**P**lus, counter-clockwise (CCW) rotation) or M (**M**inus, clockwise (CW) rotation), as shown in Fig. 1a.

Since P and M layers are translationally nonequivalent, $MoTe_2$ is a stack of P and M layers coupled through weak van der Waals forces with two possible interlayer shear displacements. Figure 1b presents schematics of these interlayer shear displacements defined by the closest Te-Te ions (dashed lines), denoted as + (positive; CCW displacement of Te-Te dashed line) or - (negative; CW displacement). 1T' and T_d phases can be defined by the stacking sequence counting from the bottom: two 1T' monoclinic twins are repeating arrangements of +M+P+ and -M-P- (1T'-I and 1T'-II, respectively in Fig. 1c), and T_d-$MoTe_2$ phase refers to stacks either as +M-P+ and -M+P- corresponding to two polar states ($T_d\uparrow$ and $T_d\downarrow$ in Fig. 1c). Note that symbols P/M represent the intra-layer displacements of Te octahedra, which remain fixed, while +/- represent the variable interlayer shifts. A T_d unit consists of +/- (i.e. different) displacements of the two sides of each layer (either P or M), while a 1T' unit has an identical interlayer displacement (either +/+ or -/- in Fig. 1c). An uncompensated dipole, resulting in polarization along the *c* axis, can exist in the $T_d\uparrow$ and $T_d\downarrow$ states due to the asymmetric Te bonding environments triggered by the interlayer shifts[35] (see Supplementary section 1 and Fig. S2). This subtle difference of 1T' and T_d phases has never been explicitly discussed and explains in part the reported sensitivity of the phases and electronic properties of $MoTe_2$ to external strain, pressure and thickness[29,30,38].

Cross-sectional view of abundant phase domain walls

Intriguingly, we find that 1T' twin walls have T_d character at room temperature. A cross-section view of 1T'-$MoTe_2$ has been imaged using dark-field transmission electron microscopy (DF-TEM) in combination with high-angle annular dark field (HAADF) scanning transmission electron microscopy (STEM) imaging, which displays strong contrast associated with the atomic number of the local composition. Figure 2a-b reveals quasi-periodic monoclinic twin domains of alternating bright and dark bands along the *c* axis, which are consistent with the superposition of diffraction spots (Fig. 2a) resulting from adjacent twin domains. 1T' twinning occurs by a mirror operation along the *ab*-plane. A further zoomed-in HAADF-STEM image of a twin wall (Fig. 2c) shows an atomically coherent interface between 1T'-I and 1T'-II along [110]. The interfaces (the blue dashed lines in Fig 2c) can be readily identified by tracking the white-circled Mo positions. The yellow and orange shaded areas outline the 1T' monoclinic unit cells above and below the interfaces. It turns out that in addition to a mirror operation, a gliding of atomic layers is imposed

on either side of the twin wall to reduce lattice strain. As a consequence, a thin planar T_d unit (- M+) emerges owing to the crystallographic glide. The existence of a T_d unit can also be understood in our notation in which the meeting region of 1T'-I (+ +, indicated by orange dashed lines) and 1T'-II (- -, indicated by purple dashed lines) along the *c* axis naturally gives a layer with - + interlayer shearing (the right panel of Fig. 2c). Thus, numerous T_d mono-layers exist at the 1T' monoclinic twin walls at room temperature.

Next, we turn our attention to the temperature-driven 1T' to T_d first-order phase transition, which manifests itself by resistivity anomalies with an evident thermal hysteresis[29,30,39] (Supplementary Fig. S1). A phase coexistence is expected within this hysteretic temperature window, but remains little explored on meso- or nano-scales. Note that a pronounced thermopower enhancement near the phase boundary was ascribed to a significant gradient of scattering processes where real-space phase inhomogeneity may play an important role[40]. To explore the real-space phase configurations, we begin with cross-section views using in-situ cryogenic-TEM. Figures 2d-e are DF-TEM images taken in the same area at 80 K ($<< T_c$) and 300 K ($> T_c$) after a cooling/warming cycle. In the DF-TEM images using the stronger spots (green arrows in Fig. 2a and Supplementary Fig. S3), the areas associated with the major 1T'-I phase exhibit a bright contrast while regions with minor 1T'-II and newly nucleated T_d phases remain dark upon cooling (from 300 K to 80 K). Interestingly, two essentially different types of periodicities consisting of alternating bright and dark stripes can be found. First, long-range stripes corresponding to two types of 1T' twin domains, exist at 300 K (Fig. 2b and Fig. 2e). At 80 K, additional short-range stripes appear inside individual twin domains (Fig. 2d). Instead of the T_d phase growth from the existing T_d units at twin walls, abundant thin-plate-like nucleation of T_d phase occurs within individual 1T' twin domains, in agreement with the appearance of additional diffraction spots (Supplementary Fig. S3).

Therefore, there appears an intimate connection between the 1T' and T_d phases, and the system enters a metastable state with significant amounts of coexisting phase domains and DWs at the thermal 1T'-T_d phase transition. The spatially modulating layers contain alternating T_d and 1T' phases, resembling artificial thin-film superlattices. An enlarged 80 K DF-TEM image and the corresponding line profile are shown in Fig. 2f. The T_d and 1T' phase modulation is rather periodic and the thinnest periodicity, 4-nm, consists of 6 layers of either T_d or 1T' unit. Possible atomic models are shown in Supplementary Fig. S4. The experimental signature of the first-order

phase transition manifests itself microscopically as a nanoscale modulation of in-phase (++/--) and anti-phase (+-/-+) interlayers with quasi-periodicity. Note that both 1T'-I and 1T'-II require a mechanical glide of the layers in opposite directions when transforming into the T_d phase (Fig. 1c). The persistent phase coexistence at 80 K implies an effect of mechanical constraints applying restoring forces that tend to resist the layer-wise gliding from its initial position, particularly in our capped cross-section TEM specimen; details are given in Supplementary Section 2.

In-plane view of polar domains and domain walls

A further identification of polar states of these thin T_d layers from cross-section views is beyond the detectability limits of our low-magnification DF-TEM technique. However, our *ab*-plane DF-TEM view reveals unambiguously the existence of two types of polar domains. Figure 3a displays the in-plane DF-TEM image of two domains with bright and dark contrasts, resulting from the non-equal diffraction intensity due to the broken space-inversion of T_d phase at 80 K. Note that no domains and DWs are found in in-plane DF-TEM images of any specimen without initial cooling at room temperature (Supplementary Figs. S5a-b). The domains with two different contrasts are associated with the ±*c* polar axes, but the absolute polarization direction cannot be identified in the *ab*-plane TEM view. Thus, for the sake of simplicity, we assign bright-contrast domains as $T_d\uparrow$ and dark-contrast domain as $T_d\downarrow$ in this work. The step-by-step phase transition during in-situ cooling is also provided in the sequential DF-images in Supplementary Figs. S6a-e. We also confirm the coexistence of 1T' and T_d phase domains during a warming cycle (Supplementary Figs. S5b-d), in which the domain contrast of 1T' phase remains intact in different imaging conditions. (More details are shown in Supplementary Fig. S5).

Manipulation of polar domains and domain walls with the electron beam

The T_d polar domains and DWs are found to be easily manipulated with in-situ TEM e^- beam at 80 K (Figs. 3a-b). The consistent and sharp domain contrast before (Fig. 3a) and after (Fig. 3b) e^- beam irradiation suggests a still non-centrosymmetric structure, i.e. T_d phase. Figures 3c show four TEM snapshots from an in-situ TEM video (Supplementary Movie 1) showing the shrinkage of a dark-contrast $T_d\downarrow$ domain, through a layer-by-layer gliding/phase-flipping process. A key feature is the observation of multi-DWs outlined by colored lines (the right panels of Fig.

3c), which represent the boundaries between domains of different volume fractions of $T_d\uparrow/T_d\downarrow$ along the *c* axis. Purple and blue shaded areas (the right panel of Fig. 3c) mark $T_d\uparrow$ dominated and $T_d\downarrow$ dominated domains, respectively. The brighter contrast appears in DF-images when the $T_d\uparrow$ volume ratio is higher. The engineering of TMD polymorphs has attracted significant interest because of minimum-energy pathways or feasible transient polymorphs triggered by charge injection[41], laser irradiation[42], mechanical strain[43] and e^- beam irradiation[44]. In the case of $MoTe_2$, despite 2H to 1T' phase change can occur by laser irradiation due to a local heating and Te vacancies[42,43] or electrostatic gating[41], however, any transition mechanism involving the 2H phase is excluded in our work because of the consistent electron diffraction pattern and domain contrast before and after e^- beam irradiation (Fig. 3a-3b and Supplementary Figs. 6f-6g). Notably, the induced domains and DWs return to their original morphology after removing the focused e^- beam. A restorative DW motion is captured by in situ videos (Supplementary Movie 2). The reversibility of $T_d\uparrow$ and $T_d\downarrow$ domains proves that there is no massive Te atom loss or damage by the knock-on effect during the exposure. The e^- beam induced domain behavior is known in ferroelectric insulators, and attributed to positive specimen charging in insulating materials[45,46]; however, no static charge accumulation is expected in semimetallic $MoTe_2$.

To understand the switching phenomena, we compute the potential energy landscape of $MoTe_2$ using first-principles density functional theory (DFT) calculations[47-51] (see Methods). As shown in Fig. 1a, the P and M layers are related by the symmetry operation $M_z \mid \left(\frac{\boldsymbol{b}}{2} + \lambda\right)$, where M_z, $\boldsymbol{b}$ and λ represent a vertical mirror, lattice vector, and the interlayer displacements between two neighboring layers, respectively. We identify a new high-symmetric orthorhombic structure T_0 (*Pnma*, S.G. 62) of $MoTe_2$ at $\lambda = 0$ (Fig. 1a) which belongs to the high-energy peak on the potential energy landscape of $MoTe_2$ (Fig. 3d). The T_0 phase has two instabilities: (1) an unstable in-plane optical phonon mode at the Brillouin zone center, and (2) an elastic instability yielding negative elastic stiffness coefficients. The first instability leads to an interlayer displacement of neighboring layers, yielding a double-well potential energy profile with two local minima at $\lambda = \pm 0.5$ Å, representing $T_d\uparrow/T_d\downarrow$ phases (Supplementary Fig. S7). The second instability causes a rigid shear of the orthorhombic unit cell, making the *b*-*c* cell angle non-orthogonal. By rotating the *b*-*c* angle of the T_0 phase, we again obtain a double-well potential energy profile having two local minima at 86.4^o and 93.6^o corresponding to 1T'-I and 1T'-II phases, and the predicted monoclinic angle is in good agreement with the experimental data (93.5^o - 93.9^o) [30,37,52]. This

monoclinic distortion has the effect of shifting the neighboring layers horizontally, by about the same distance as in the T_d phases, suggesting that it is driven by the same underlying microscopic instability.

Figure 3d shows the potential energy surface of $MoTe_2$ in the vicinity of the T_0 phase as a function of λ and the *b*-*c* angle. We obtain four minima corresponding to T_d↑, T_d↓, 1T'-I, and 1T'-II phases, where the T_d phases are the lowest in energy with reference to the high-energy point T_0. A direct structural transition from the T_d↑ to T_d↓ (1T'-I to 1T'-II) phase through the peak along path-1 (path-2), as shown in Fig. 3d, requires overcoming a large energy barrier of height 16.9 meV/u.c. (13.5 meV/u.c.). However, there are lower-energy pathways with an energy barrier of ~5 meV/u.c., marked as path-3 in Fig. 3d, suggesting that the T_d↑ to T_d↓ polar converting *via* an intermediate nonpolar 1T' phase is energetically preferable. In this respect, a feasible low energy path through the 1T' DW-mediated switching process may be involved in our e^- beam effect. The electron beam is certainly required to trigger the layer shearing.

Phase domain wall conductance

Finally, the atomic-scale electronic properties of lateral polar and phase DWs are also investigated by scanning tunneling microscopy (STM). In order to increase the density of polar and phase domains and DWs in the *ab*-plane, we have grown Fe-doped $MoTe_2$ crystals (see Methods). One polar/phase junction among T_d↑, T_d↓ and 1T' domains is found at 77 K (Fig. 4a) in a $MoTe_2$:Fe crystal with a slightly lower phase transition temperature (Supplementary Fig. S1). Consistent with the identical nature of each layer of 1T' and T_d phases discussed above, three domains near the junction present similar topography and spectroscopic features as well as quasiparticle interference patterns, which are dominated by the atomic distribution of Fe dopants (the details are given in Supplementary Figs. S1 and S8). On the other hand, DWs reveal two different types; the first-type is marked with red and green dots in Fig. 4a-b), which deviates from the zigzag direction, i.e. the *a*-axis direction. The zigzags, corresponding to high-intensity lines in Fig. 4c, shift in the direction perpendicular to zigzags at the protruded area (red-dot DW) (Fig. 4c). On the other hand, the second-type DW follows the zigzag direction (Fig. 4a-b blue). The shift at the first-type DWs is likely due to the mismatch of the unit cell between monoclinic 1T' and orthorhombic T_d phase domains. These considerations lead to the most likely domain assignment shown in Fig. 4a. From our TEM and STM observations, we find that polar DWs

tend to be parallel along the zigzag direction while phase DWs tend to be highly curved (Fig. 3c and Supplementary Fig. S6).

Interestingly, from tunneling spectroscopy measurements, we observe characteristic local density of states at these two types of DWs, distinct from that of the bulk (Fig. 4d). The first-type protruded DWs, namely 1T'/T_d phase DWs, (Fig. 4d red and green curves) show an enhanced conductance in the empty state while the second-type DW (Fig. 4d blue curve) does in the filled state. These features are also apparent in spatial mapping of conductance taken at filled (-100 mV, Fig. 4e) and empty (+100 mV, Fig. 4f) states. The systematic studies of spatial variation of local density of states are given in Supplementary Fig. S9. Our results demonstrate distinct electronic properties at those polar and phase DWs in $MoTe_2$. Note that 1T'-$MoTe_2$ was earlier considered to be a topologically trivial material[17,18,37] based on the Fu-Kane Z_2 index criterion[53], however, recent theoretical works predict that 1T'-$MoTe_2$ inherits a higher order topological phase featuring topologically protected 1D hinge modes at the edges[32-34]. We notice that a considerably large conductance at the first-type 1T'/T_d phase DWs with the orientation-dependent feature (Fig. 4d red and green curves). Alternatively, those protruded type 1T'/T_d DWs can be promising candidates for the conducting hinge state studies in future[54].

Conclusions and outlook:

In summary, for the first time we report the existence of polar domains and abundant superlattice-like arrangements of phase DWs in $MoTe_2$ using in-situ cryogenic TEM along planar and cross-section views. We also discuss the feasible low-energy pathways of the polar domain switching. Our observations open up several important directions for future exploration. First, notably, the T_d polar phases of $MoTe_2$ hosts topologically non-trivial Weyl points[17,18,36,37]. Since $T_d\uparrow$ and $T_d\downarrow$ polar phases are related by the space-inversion symmetry, Weyl points in these phases will have the same location in the energy and momentum space, but opposite chirality. Thus, a tunable topological Weyl switch can be realized in a single material having two polar variant phases. It would also be interesting to study the quantum phenomena occurring due to the projection of opposite pairs of Weyl points and resulting Fermi arc patterns at the $T_d\uparrow/T_d\downarrow$ polar DWs. The observed interfacial states at the phase DWs of topologically nontrivial WSM and high-order topological phases (T_d/1T' superlattice structures along the *c* axis) call for further attention. In addition, our STM observations imply the possible presence of conducting hinge

states in the protruded type 1T'/T_d phase DWs. Second, those Td/1T' superlattice regions with abundant phase DWs can be described as a transient state which may be a rich area for macro-scale ordering by modulating the interlayer stacking and topological invariant. Lastly, the existence of polar domains and the electron beam manipulation of those polar DWs offer the possibility of rapid/controllable topological switching through electronic/optical excitations[26] and could be extended to other WSM or polar metals.

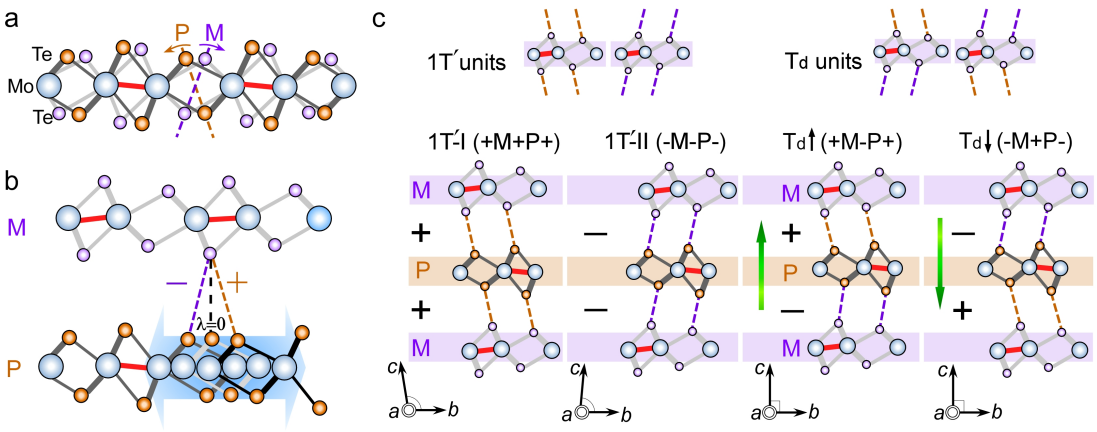

Figure 1 (double column) Flexible layer-structured $MoTe_2$. a, Schematic models of a single layer of $MoTe_2$ with either P (Plus, CCW rotation) or M (Minus, CW)-type Te octahedral deformations in the cross-section view. Mo, blue; Te of P-layer, orange; Te of M-layer, purple. The red lines indicate Mo-Mo zigzags along the *a* axis. Orange and purple curved arrows represent the directions of the Te octahedral deformations. **b**, Schematic models of bilayer $MoTe_2$ with P-M and P+M configurations, counting from the bottom P layer. Gliding of the bottom P layer results in + (positive)/– (negative) interlayer shifts, where the sign refers to a CCW/CW displacement of Te-Te bonding lines. A zero interlayer shear ($\lambda = 0$) corresponds to a centrosymmetric orthorhombic reference structure T_0. **c**, Top, examples of 1T' and T_d units of a M layer. A 1T' unit requires the same sign of interlayer shearing (++ or --) while those of a T_d unit are different. Bottom, three layers can glide individually to give four configurations. (1) 1T'-I, +M+P+ with *b*-*c* angle of ~93.5° and (2) 1T'-II, -M-P- with *b*-*c* angle of ~86.5°;[52] (3) T_d↑, +M-P+ and (4) T_d↓, -M+P- with orthogonal unit cells. The polarization along the ±*c* axis (green

arrows) denotes as T_d↑ and T_d↓. Note that lattice *a* and *b* of the 1T' structure are switched to match the zigzag direction as in the T_d phase.

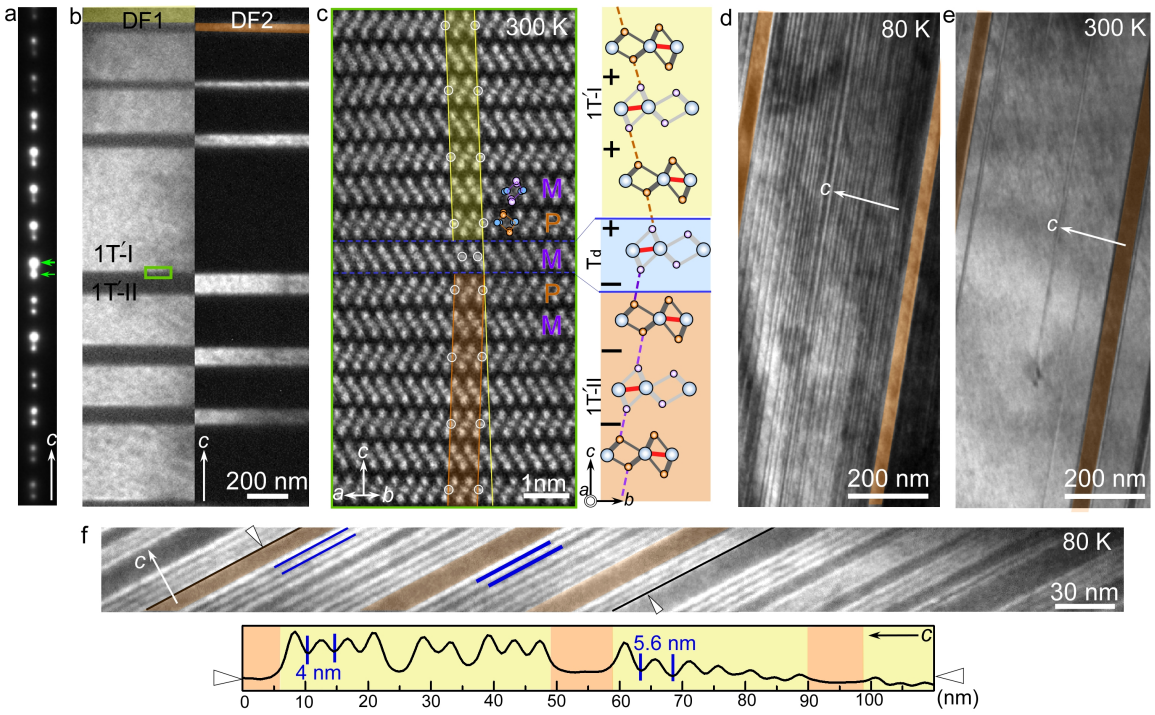

Figure 2 (double columns) Phase domain walls along cross-section views at room and cryogenic temperatures. a, Selected area electron diffraction (SAED) pattern of 1T' monoclinic twins, revealing spot splitting along *c* axis. **b,** DF-images were taken using the strong and weak $(1\bar{1}2)$ spots (green arrows) of variants 1T'-I and 1T'-II, denoted as DF1 and DF2, respectively. Yellow and orange false colors are added to aid the eye. The average twin width is on the order of a half-μm, and the two types of twin domains are typically unequal in size. **c**, Atomic-resolved HAADF-STEM image over one twin wall along the [110] zone axis. Overlaid color-coded 1T' unit cells defined by white-circled Mo atomic columns show a glide-reflection twin. The twin is composed of one M layer (marked by blue dashed lines) with anti-phase (+ -) interlayer shearing, connecting 1T'-I (yellow-shaded) and 1T'-II (orange-shaded) regions. The lattice model viewed along [100] is shown for clarity. **d**, **e**, DF-images taken at (**d**) 80 K and (**e**) 300 K. At 80 K, the phase-separated state is observed. The appearance of thin T_d layers within the initial 1T' twins, revealing additional $(1\bar{1}2)$ spots due to an orthogonal T_d unit-cell as shown in Supplementary Fig. S3. **f**, Top, a higher-magnification DF-image, showing superlattice-like $-(T_d)_m(1T')_n-$ (m, n =

integer) nanoscale phase DWs at 80 K. Bottom, the intensity profile between white arrow heads along the *c* direction, covering both 1T'-I (yellow) and 1T'-II (orange) twins. The image is rotated and enlarged to enhance the display.

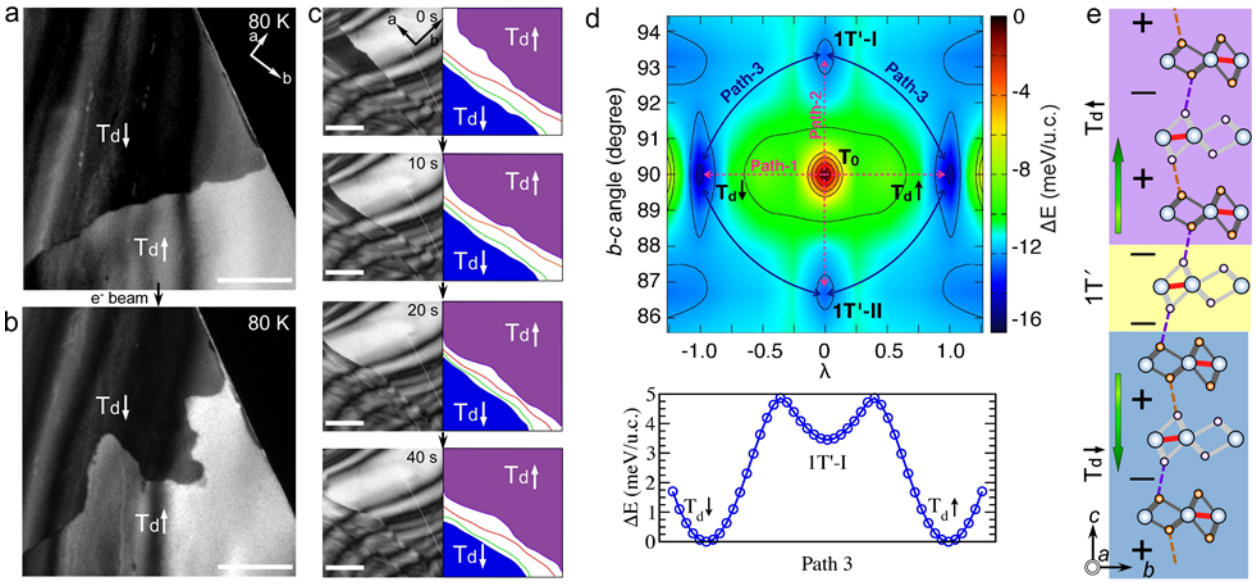

Figure 3 (double columns) Polar domain and domain wall kinetics under e⁻ beam along plane views at 80 K. a, DF-image of two T_d domains with bright and dark contrasts. **b**, An immediate DF-TEM image of the same area after exposure to a focused e^- beam, showing DW motion accompanying the shrinkage of the dark-contrast $T_d\downarrow$ domain. **c**, Sequential snapshots obtained from the in-situ video, revealing representative polar DW motions after exposure to a focused **e⁻** beam. Four visible DWs are outlined in purple, red, green and blue, which represent the DWs between gradient domains of different $T_d\uparrow/T_d\downarrow$ volume fractions along *c* axis. The $T_d\uparrow$ dominated (purple-shaded) domain is favored and expanded under electron beam while the $T_d\downarrow$ dominated (blue-shaded) domain has shrunk. Scale bar, 500 nm. **d**, Top panel shows the potential energy surface as a function of the normalized interlayer displacement (λ) and *b*-*c* cell angle. Color scale denotes energy with respect to the high-energy peak T_0 phase. Bottom panel depicts $T_d\downarrow$ to $T_d\uparrow$ transition energy profile along the lowest energy path-3. **e**, Schematic model of a $T_d\uparrow$ (purple-shaded) and $T_d\downarrow$ (blue-shaded) junction along *c* axis, containing one 1T' unit (yellow-shaded) as bridge.

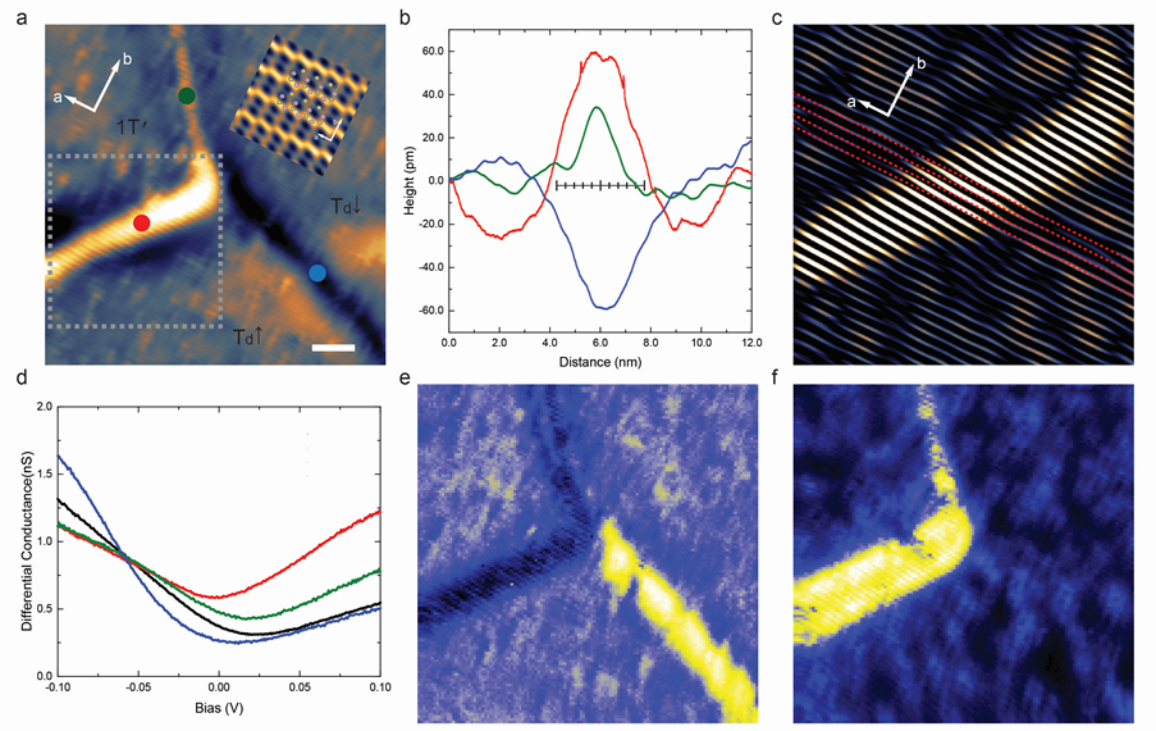

Figure 4. (double columns) STM spectroscopic features of lateral phase domains and DWs in $MoTe_2$:Fe. **a**, STM topography showing a junction of three domains and DWs. Inset: atomic resolution image of $MoTe_2$ showing Mo-Te-Mo chains. Scale bar: 5 nm. **b**, Height profile across each of three DWs obtained from red, green and blue dots in (**a**). Red and green represent the first-type protruded DWs and blue belongs to the second-type. A ruler at the center shows the length of ten unit cells for comparison. **c**, Fourier filtered topography of the first-type DW from the dashed rectangle in (**a**). Red dashed lines mark ideal chain directions and the topography on the protruded area reveals the deviation of chain from the ideal straight line. **d,** Differential conductance obtained from each DW in (**a**). Red and green curves: the first-type protruded DWs; Blue curve: the second-type depressed DW; Black: the averaged curve obtained inside a domain, normalized at -100 mV, 100 pA. **e**,**f**, Spatial mapping of differential conductance at -100 mV (**e**) and +100 mV (**f**), normalized at -50 mV, 100 pA.

Methods

Sample preparation

1T'-$MoTe_2$ single crystals were grown using the flux method. Well ground Mo (Alfa Aesar, 99.9 %) and Te (Alfa Aesar, 99.9 %) powders were mixed with sodium chloride (NaCl, Alfa Aesar, 99.9 %) in an alumina crucible, which was sealed in a quartz tube under vacuum. Crystallization

was conducted from 1100 to 960 ^{o}C for 12 hrs, following a 0.5 ^{o}C/h cooling rate to 960 ^{o}C and then a rapid cooling to room temperature by placing the quartz tube in water (quenching). Ribbon-like crystals (3*0.5*0.1 mm^3) with shiny surfaces were obtained. 1T'-$MoTe_2$:Fe single crystals were grown using a similar process with the starting composition of $Fe_{0.3}MoTe_2$, but tends to form ten times smaller in size and less cleavability. From the analysis of STM images, the real Fe concertation is found to be 1.06 %. The electrical transport measurements (along the *b* axis) were taken with the standard four-probe technique using Au paste as electrodes. Temperature was controlled by using a Physical Properties Measurement System (PPMS-9, Quantum Design), are consistent with the results in literature[29,30].

TEM measurement

Crystal structure, electron diffraction and domains were examined by transmission electron microscopy (TEM) in side view and plane view. Plane-view specimens were obtained by scotch-tape exfoliation, while side-view specimens were fabricated as follows. First, two silicon slabs and one $MoTe_2$ thin plate were clamped and glued together using epoxy bond (Allied, Inc) with sides facing each other to make a sandwich structure. The $MoTe_2$ sandwich was further thinned down by mechanical polishing, followed by Ar-ion milling, and studied using a JEOL-2010F field-emission TEM quipped with a low-T sample stage and a room-T double-tilt sample stage. We observed in-plane polar domains by DF-TEM imaging taking $g_1\pm = \pm(1, 2, \bar{1})$ spots along [101] direction, ~14^{o} tilting from [001] zone and the side-view twin domains using $g_2\pm = \pm(1, \bar{1}, 2)$ spots along [110] direction, ~60^{o} tilting from [100] zone. HAADF-STEM imaging with atomic-column resolution was carried out using the field-emission JEOL-2100F microscope equipped with a spherical aberration Cs corrector. All images are raw data. HAADF-STEM images were acquired in two conditions: 512×512 with 0.019 nm and 0.015 nm/pixel with collection angle between 80-210 mrad.

STM measurements

STM and spectroscopy measurements were performed at liquid nitrogen temperature using a Unisoku ultra-high vacuum SPM System (USM-1500) with a cleaving stage in the chamber. A Cu(111) sample that is cleaned by repeated cycles of sputtering and annealing prior to scanning has been used as a reference sample. A Pt/Ir tip is heated by electron beam bombardment in ultra-high vacuum condition to remove contaminations from air, and further treated on Cu(111) sample until it shows a metallic conductivity and the Cu(111) surface state spectroscopy. Fe

doped $MoTe_2$ sample is fixed at a sample plate by silver epoxy (Epotek H20E) and a metal post is attached to the top with the same epoxy. Then the sample is introduced to ultra-high vacuum chamber and cleaved at room temperature in the cleaving stage followed by insertion to LN_2 cooled STM head. Differential conductance is measured by modulation of bias and demodulation of tunneling current using lock-in technique. (f = 611Hz, 10 mV with AC added to the bias).

Theoretical calculations

All the first-principles DFT calculations were performed using the Vienna ab initio simulation package (VASP) within the projected-augmented wave (PAW) framework[47,48]. We considered 6 valence electrons of Mo ($4d^5 5s^1$) and 6 valence electrons of Te ($5s^2 5p^4$) in the PAW pseudopotential. We used the PBEsol exchange-correlation functional to treat exchange and correlation effects[49]. A Monkhorst-Pack *k* mesh of size 8×12×4 was used to sample the *k*-space, and 600 eV was used as the kinetic energy cutoff of the plane wave basis set. We also considered effects due to the on-site Coulomb interaction of Mo 4*d* electrons, which were recently reported to be crucial in the precise determination of electronic structure of $MoTe_2$ near the Fermi-level. Within the DFT+U scheme, we used U = 2.4 eV and J = 0.4 eV to simulate Mo 4d electrons at the mean-field level. These values are reported to correctly describe the topological phase transitions and bulk electronic band structure of $MoTe_2$ near the Fermi-level[50]. The structures were optimized until the Hellmann-Feynman residual forces were less than 10^{-4} eV/Å, and 10^{-9} eV was defined as the convergence criterion for the electronic self-consistent calculations. Optimized lattice parameters and structural details are given in the Supplementary Table 1. Given the symmetry of 1T' and T_d structures, *a* and *b* lattice vectors are interchangeable. In the DFT calculations, we used a convention in which Mo-Mo zigzag run along the *b*-lattice vector (*a* > *b*). The phonon calculations were performed using the finite-difference approach as implemented in the VASP software. Supercell of size 2×4×1 was used for phonon calculations, and PHONOPY code was used for the post-processing of phonons[51]. All the inner-coordinates of atoms were fully optimized, except for the modulated structures along the unstable phonon mode at Γ, which were optimized while keeping the coordinates of atoms frozen in the direction of modulation vector. However, $T_d\uparrow$ and $T_d\downarrow$ structures were further optimized without any constraints.

Acknowledgements

The work at Rutgers was funded by the Gordon and Betty Moore Foundation's EPiQS Initiative through Grant GBMF4413 to the Rutgers Center for Emergent Materials and by NSF DMREF Grant No. DMR-1629059.

Author contributions

F.T.H. conducted the TEM experiments. S.J.L. carried out the STM observations. S.S., J.K., K.R. and D.V. carried out the theoretical analysis. J.W.K. performed transport measurements. L.Z. synthesized single crystals. F.T.H. and M.W.C performed the STEM observations. F.T.H., S.J.L., S.S., D.V. and S.W.C. wrote the manuscript. S.W.C. initiated and supervised the research.

Data availability

The authors declare that all source data supporting the findings of this study are available within the article and the Supplementary Information File.

Competing interests

The authors declare no competing financial interests.

References

1. Bradlyn, B. *et al.* Topological quantum chemistry. *Nature* **547,** 298–305 (2017).
2. Yan, B. & Felser, C. Topological materials: Weyl semimetals. *Annu. Rev. Condens. Matter Phys.* **8,** 337–354 (2017).
3. Armitage, N. P., Mele, E. J. & Vishwanath, A. Weyl and Dirac semimetals in three-dimensional solids. *Rev. Mod. Phys.* **90,** 015001 (2018).
4. Hasan, M. Z., Xu, S.-Y., Belopolski, I. & Huang, S.-M. Discovery of Weyl fermion semimetals and topological Fermi arc states. *Annu. Rev. Condens. Matter Phys.* **8,** 289–309 (2017).
5. Xu, S.-Y. *et al.* Discovery of a Weyl fermion semimetal and topological Fermi arcs. *Science* **349,** 613–617 (2015).
6. Zyuzin, A. A., Wu, S. & Burkov, A. A. Weyl semimetal with broken time reversal and inversion symmetries. *Phys. Rev. B* **85,** 165110 (2012).
7. Chen, A. & Franz, M. Superconducting proximity effect and Majorana flat bands at the surface of a Weyl semimetal. *Phys. Rev. B* **93,** 201105 (2016).
8. O'Brien, T. E., Diez, M. & Beenakker, C. W. J. Magnetic breakdown and Klein tunneling in a type-II Weyl semimetal. *Phys. Rev. Lett.* **116,** 236401 (2016).
9. Grushin, A. G. & Bardarson, J. H. How to make devices with Weyl materials. *Phys. Today* **10,** 63 (2017).

10. Li, X.-S., Zhang, S.-F., Sun, X.-R. & Gong, W.-J. Double Andreev reflections and double electron transmissions in a normal-superconductor-normal junction based on type-II Weyl semimetal. *New J. Phys.* **20,** 103005 (2018).
11. Edmonds, M. T. *et al.* Stability and surface reconstruction of topological insulator Bi_2Se_3 on exposure to atmosphere. *J. Phys. Chem. C* **118,** 20413–20419 (2014).
12. Mahatha, S. K. *et al.* Silicene on Ag(111): A honeycomb lattice without Dirac bands. *Phys. Rev. B* **89,** 201416 (2014).
13. Lee, C.-H. *et al.* Tungsten ditelluride: a layered semimetal. *Sci. Rep.* **5,** 10013 (2015).
14. Butler, C. J. *et al.* Mapping polarization induced surface band bending on the Rashba semiconductor BiTeI. *Nat. Commun.* **5,** 4066 (2014).
15. Ugeda, M. M. *et al.* Observation of topologically protected states at crystalline phase boundaries in single-layer WSe2. *Nat. Commun.* **9,** 3401 (2018).
16. Yin, L.-J., Jiang, H., Qiao, J.-B. & He, L. Direct imaging of topological edge states at a bilayer graphene domain wall. *Nat. Commun.* **7,** 11760 (2016).
17. Sun, Y., Wu, S.-C., Ali, M. N., Felser, C. & Yan, B. Prediction of Weyl semimetal in orthorhombic $MoTe_2$. *Phys. Rev. B* **92,** 161107 (2015).
18. Jiang, J. *et al.* Signature of type-II Weyl semimetal phase in MoTe2. *Nat. Commun.* **8,** 13973 (2017).
19. Wu, L. *et al.* Giant anisotropic nonlinear optical response in transition metal monopnictide Weyl semimetals. *Nat. Phys.* **13,** 350–355 (2017).
20. Xu, S.-Y. *et al.* Discovery of Lorentz-violating type II Weyl fermions in LaAlGe. *Sci Adv* **3,** e1603266 (2017).
21. Chang, G. *et al.* Magnetic and noncentrosymmetric Weyl fermion semimetals in the RAlGe family of compounds (R = rare earth). *Phys. Rev. B* **97,** 041104 (2018).
22. Benedek, N. A. & Birol, T. 'Ferroelectric' metals reexamined: fundamental mechanisms and design considerations for new materials. *J. Mater. Chem. C* **4,** 4000–4015 (2016).
23. Shi, Y. *et al.* A ferroelectric-like structural transition in a metal. *Nat. Mater.* **12,** 1024–1027 (2013).
24. Kim, T. H. *et al.* Polar metals by geometric design. *Nature* **533,** 68–72 (2016).
25. Dwivedi, V. Fermi arc reconstruction at junctions between Weyl semimetals. *Phys. Rev. B* **97,** 064201 (2018).
26. Sie, E. J. *et al.* An ultrafast symmetry switch in a Weyl semimetal. *Nature* **565,** 61–66 (2019).
27. Iaia, D. *et al.* Searching for topological Fermi arcs via quasiparticle interference on a type-II Weyl semimetal $MoTe_2$. *npj Quantum Mater.* **3**, 38 (2018).
28. Sakano, M. *et al.* Observation of spin-polarized bands and domain-dependent Fermi arcs in polar Weyl semimetal MoTe2. *Phys. Rev. B* **95,** 121101–6 (2017).
29. Yang, J. *et al.* Elastic and electronic tuning of magnetoresistance in $MoTe_2$. *Sci Adv* **3,** eaao4949 (2017).
30. Heikes, C. *et al.* Mechanical control of crystal symmetry and superconductivity in Weyl semimetal $MoTe_2$. *Phys. Rev. Mater.* **2,** 074202 (2018).
31. Qi, Y. *et al.* Superconductivity in Weyl semimetal candidate $MoTe_2$. *Nat. Commun.* **7,** 11038 (2016).
32. Tang, F., Po, H. C., Vishwanath, A. & Wan, X. Efficient topological materials

discovery using symmetry indicators. *Nat. Phys.* (2019). https://doi.org/10.1038/s41567-019-0418-7

33. Wang, Z., Wieder, B. J., Li, J., Yan, B. & Bernevig, B. A. Higher-order topology, monopole nodal lines, and the origin of large fermi arcs in transition metal dichalcogenides XTe_2 (X=Mo,W). *arXiv.v* 1806.11116 (2018).
34. Ezawa, M. Second-order topological insulators and loop-nodal semimetals in Transition Metal Dichalcogenides XTe2 (X = Mo, W). *Sci. Rep.* **9,** 5286 (2019).
35. Yang, Q., Wu, M. & Li, J. Origin of two-dimensional vertical ferroelectricity in WTe_2 bilayer and multilayer. *J. Phys. Chem. Lett.* **9,** 7160–7164 (2018).
36. Wang, Z. *et al.* $MoTe_2$: A type-II Weyl topological metal. *Phys. Rev. Lett.* **117,** 056805 (2016).
37. Tamai, A. *et al.* Fermi arcs and their topological character in the candidate type-II Weyl semimetal $MoTe_2$. *Phys. Rev. X* **6,** 031021 (2016).
38. Keum, D. H. *et al.* Bandgap opening in few-layered monoclinic $MoTe_2$. *Nat. Phys.* **11,** 482–486 (2015).
39. Yan, X.-J. *et al.* Investigation on the phase-transition-induced hysteresis in the thermal transport along the c-axis of $MoTe_2$. *npj Quantum Mater.* **2,** 31 (2017).
40. Sakai, H. *et al.* Critical enhancement of thermopower in a chemically tuned polar semimetal $MoTe_2$. *Sci Adv* **2,** e1601378 (2016).
41. Wang, Y. *et al.* Structural phase transition in monolayer $MoTe_2$ driven by electrostatic doping. *Nature* **550,** 487–491 (2017).
42. Cho, S. *et al.* Phase patterning for ohmic homojunction contact in $MoTe_2$. *Science* **349,** 625–628 (2015).
43. Yang, H., Kim, S. W., Chhowalla, M. & Lee, Y. H. Structural and quantum-state phase transition in van der Waals layered materials. *Nat. Phys.* **13,** 931–937 (2017).
44. Lin, Y.-C., Dumcenco, D. O., Huang, Y.-S. & Suenaga, K. Atomic mechanism of the semiconducting-to-metallic phase transition in single-layered MoS_2. *Nat. Nanotechnol.* **9,** 391–396 (2014).
45. Hart, J. L. *et al.* Electron-beam-induced ferroelectric domain behavior in the transmission electron microscope: Toward deterministic domain patterning. *Phys. Rev. B* **94,** 174104 (2016).
46. Chen, Z., Wang, X., Ringer, S. P. & Liao, X. Manipulation of nanoscale domain switching using an electron beam with omnidirectional electric field distribution. *Phys. Rev. Lett.* **117,** 027601 (2016).
47. Kresse, G. & Furthmuller, J. Efficient iterative schemes for ab initio total-energy calculations using a plane-wave basis set. *Phys. Rev. B* **54,** 11169–11186 (1996).
48. Kresse, G. & Joubert, D. From ultrasoft pseudopotentials to the projector augmented-wave method. *Phys. Rev. B* **59,** 1758–1775 (1999).
49. Perdew, J. P. *et al.* Restoring the density-gradient expansion for exchange in solids and surfaces. *Phys. Rev. Lett.* **100,** 136406 (2008).
50. Xu, N. *et al.* Evidence of a coulomb-interaction-induced Lifshitz transition and robust hybrid Weyl semimetal in T_d-$MoTe_2$. *Phys. Rev. Lett.* **121,** 136401 (2018).
51. Togo, A., Oba, F. & Tanaka, I. First-principles calculations of the ferroelastic transition between rutile-type and $CaCl_2$-type SiO_2 at high pressures. *Phys. Rev. B* **78,** 134106 (2008).
52. Clarke, R., Marseglia, E. & Hughes, H. P. A low-temperature structural phase

transition in β-$MoTe_2$. *Philosophical Magazine B* **38,** 121–126 (1978).
53. Fu, L. & Kane, C. L. Topological insulators with inversion symmetry. *Phys. Rev. B* **76,** 045302 (2007).
54. Schindler, F. *et al.* High-order topology in bismuth. *Nat. Phys.* **14,** 918 (2018).